Journal of the Korean Astronomical Society
52: 227 ∼ 233, 2019 December

https://doi.org/10.5303/JKAS.2019.52.6.227
pISSN: 1225-4614 · eISSN: 2288-890X
http://jkas.kas.org

# Performance of the TRAO 13.7-m Telescope with New Systems

Il-Gyo Jeong[1,2], Hyunwoo Kang[1], Jaehoon Jung[1], Changhoon Lee[1], Do-Young Byun[1,3], Do-Heung Je[1], Sung-Ju Kang[1], Youngung Lee[1], and Chang Won Lee[1]

[1]Korea Astronomy and Space Science Institute 776, Daedeokdae-ro, Daejeon, Korea
igjeong@kasi.re.kr, orionkhw@kasi.re.kr
[2]SETsystem, Inc., 4th Floor Hongnam BD, 16-3, Gangnam-daero 8-gil, Seocho-gu, Seoul, Korea
[3]University of Science and Technology, 217 Gajeong-ro, Yuseong-gu, Daejeon 34113, Korea

Received September 27, 2019; accepted December 5, 2019

**Abstract:** We report the performance of the 13.7-meter Taeduk Radio Astronomy Observatory (TRAO) radio telescope. The telescope has been equipped with a new receiver, SEQUOIA-TRAO, a new backend system, FFT2G, and a new VxWorks operating system. The receiver system features a 16-pixel focal plane array using high-performance MMIC preamplifiers; it shows very low system noise levels, with system noise temperatures from 150 K to 450 K at frequencies from 86 to 115 GHz. With the new backend system, we can simultaneously obtain 32 spectra, each with a velocity coverage of 163 km s$^{-1}$ and a resolution of 0.04 km s$^{-1}$ at 115 GHz. The new operating system, VxWorks, has successfully handled the LMTMC-TRAO observing software. The main observing method is the on-the-fly (OTF) mapping mode; a position-switching mode is available for small-area observations. Remote observing is provided. The antenna surface has been newly adjusted using digital photogrammetry, achieving a rms surface accuracy better than 130 $\mu$m. The pointing uncertainty is found to be less than 5″ over the entire sky. We tested the new receiver system with multi-frequency observations in OTF mode. The aperture efficiencies are 43±1%, 42±1%, 37±1%, and 33±1%, the beam efficiencies are 45±2%, 48±2%, 46±2%, and 41±2% at 86, 98, 110, and 115 GHz, respectively.

**Key words:** telescopes — instrumentation: miscellaneous — techniques: photometric, spectroscopic — methods: observational

## 1. Introduction

The 13.7-meter radio telescope of the Taeduk Radio Astronomy Observatory (TRAO) was established in 1986 on the campus of the Korea Astronomy and Space Science Institute (KASI) in Daejeon, South Korea. Since its opening, the TRAO has supported the radio astronomy community in Korea and begun a new era of millimeter radio astronomy. The main research areas using the TRAO telescope are molecular clouds, star formation activities, supernova remnants, line surveys, and evolution studies of late-type stars (Cho et al. 1998, 2007; Koo et al. 2001; Loughnane et al. 2012; Lee et al. 2014).

As part of continuous efforts to improve the observatory's environment, the TRAO has been upgraded to match the requirements of current radio astronomy research (i.e., low signal-to-noise ratio, high spectral resolution, and wideband systems). The new receiver, the SEcond QUabbin Observatory Image Array-TRAO (SEQUOIA-TRAO) with a 4×4 array (Erickson et al. 1999), and related systems, shows substantially improved performance over the previous system, the Quabbin Array (QUARRY). QUARRY was equipped with 3×5 Schottky diode mixers covering a frequency range from 85 to 115 GHz (Erickson et al. 1992); however, its system noise temperature ranged from 750 to 900 K and it was connected to a digital correlator with only 512 channels. SEQUOIA-TRAO was the receiver installed on the Five College Radio Astronomy Observatory (FCRAO) 14-m telescope for several years, but the old local oscillator (LO) was replaced with a new one. Likewise, many facility instruments were transferred to and adopted for TRAO. Additional substitutions include a servo system, a backend, a new radome, and an operating system to improve the tracking accuracy of the telescope and the data quality.

In this paper, we introduce the new observing systems and present their performance. In Section 2, we introduce the TRAO telescope and describe the new systems. Section 3 presents the beam parameter values of the TRAO telescope. Observational results obtained with the newly installed systems are presented in Section 4, and a brief summary of the results is given in Section 5.

Corresponding author: H. Kang

## 2. Upgraded Telescope Systems

### 2.1. Telescope

The TRAO telescope is a Cassegrain antenna with a 13.7-meter paraboloidal main reflector with a 1.1-meter hyperbolic sub-reflector mounted on an altitude-azimuth mount in a radome (Figure 1). The focal length and focal ratio of the telescope are 5.08 m and 0.37, respectively. The main reflector consists of 72 aluminum panels with two different shapes placed in two circumferential rows supported by four adjusters at the corners of individual panels. We used digital photogrammetry to adjust the

**Figure 1.** The TRAO 13.7-meter radio telescope.

panels and to align them with a parabolic surface. Measurements before the adjustment found a rms surface accuracy of $< 150$ $\mu$m, and Lee et al. (2014) found that the variation of beam efficiencies as a function of elevation angle was less than 3%. After adjustment, the rms surface accuracy was measured to be $< 130$ $\mu$m, thus showing a clear improvement.

In 2017, we replaced the old servo system with a new one, leading to an improved tracking accuracy with errors $< 1''$. We derived pointing model parameters by observing bright SiO maser ($v = 1$, $J = 2 - 1$) sources at 86 GHz in an elevation range of 20° to 85° using horn 7 of the new receiver as reference pixel. After applying the new pointing model, the pointing accuracy was estimated to be better than $5''$ in both azimuth and elevation directions, corresponding to $\sim$1/12 of the half-power beam width (HPBW) at 86 GHz. This outcome ensures that the gain uncertainty due to pointing errors is less than 5% for a compact source.

### 2.2. Receiver

We installed a new receiver, the SEQUOIA-TRAO, which had been developed and used by the FCRAO. It features a 16-pixel focal plane array designed to operate in the frequency range 85–115.6 GHz using cryogenic indium phosphide (InP) monolithic microwave integrated-circuit (MMIC) preamplifiers (Erickson et al. 1999). The full SEQUOIA system of the FCRAO consists of two 4×4 pixel arrays and can observe 4×4 points on the sky in both vertical and horizontal polarization at the same time. Since only a single 4×4 pixel receiver was installed at the TRAO, the SEQUOIA-TRAO can receive only single linear polarization signals. Sixteen square corrugated feed horns with an aperture size of 25 mm are closely packed, resulting in a beam spacing of 1.7–2.3 × FWHM on the sky from the lowest to highest frequencies.

In each pixel, an intermediate frequency (IF) preamplifier is integrated into a single-sideband (SSB) mixer with an IF band covering 5–20 GHz. A new first local oscillator (LO) module was developed for SEQUOIA-TRAO, generating 40.2 or 60.3 GHz signals. By selecting the LO frequency, we can select the observing frequency band from among low (85–100 GHz) and high (100–115 GHz) frequency bands. The preamplifiers are followed by a down-converter system with two LO signal generators to select two frequencies simultaneously. Finally, the output of 32 IFs can be acquired by the backend system. Figure 2 shows a simple sketch of the receiver, and Erickson et al. (1999) provide more detailed information about the system. The typical receiver noise temperatures were measured and found to be between 50 and 100 K over the range of frequencies available. The annual TRAO observing season begins in September and ends in April. During this time, levels of precipitable water vapor (PWV) are below 20 mm, providing sufficiently good observing conditions. During the winter season from December to February, the typical system noise temperature is 150–300 K and the zenith optical depth is 0.07–0.14 in the frequency range 86–110 GHz; system temperature and zenith optical depth are 450–550 K and 0.30–0.35 around 115 GHz. Outside the winter season, the typical system noise temperature is 180–350 K and zenith optical depths are 0.11–0.22 over the frequency range 86–110 GHz; at around 115 GHz, the values are 500–700 K and 0.33–0.43, respectively. About 15% of the total observing time is affected by high system temperatures due to bad weather (rain, snow). Compared to the previous receiver system, the new system improved the system temperature by a factor of two during the winter season and thus reduced the observing time by a factor of four for each pixel.

**Table 1**
Specifications of the TRAO 13.7-m telescope

| | |
|---|---|
| Location | Daejeon, Republic of Korea |
| Longitude | 127°22′30.6″E |
| Latitude | 36°23′51.2″N |
| Altitude | 144 m |
| Telescope | |
| Primary Reflector | 13.72 m |
| Subreflector Diameter | 1.09 m |
| Focal Length | 5.08 m |
| Focal Ratio (f/D) | 0.37 |
| Surface Accuracy | <130 $\mu$m |
| Mount | Alt-Az mount |
| Az. range | 5–550° |
| El. range | 11–85°.7 |
| Tracking Accuracy | <1″ |
| Pointing Accuracy | <5″ |
| Receiver | |
| SEQUOIA-TRAO | 4×4 array |
| Frequency Range | 85.0–115.6 GHz |
| Polarization | Single linear |
| Backend | FFT2G spectrometer |
| Bandwidth | 62.5 MHz |
| Channels | 4096 channels |
| Spectral resolution | 15 kHz |
| Observation modes | OTF, PS |

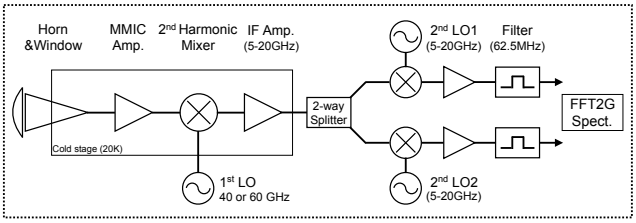


**Figure 2.** Block diagram of a single horn of the receiver.

### 2.3. Backend

In order to make use of the 32 IF outputs from the new receiving system, we introduced a new spectrometer, FFT2G, manufactured by Omnisys Instruments.[1] The FFT2G spectrometer consists of four modules. Each module can process eight input signals with bandwidths of 125 MHz in 8192 spectral channels. Because the current IF output bandwidth of the down-converter is 62.5 MHz, only 4096 channels of the backend system are available. The spectral resolution is about 15 kHz, corresponding to a velocity resolution of approximately 0.04 $\mathrm{km\,s^{-1}}$. The spectral resolution is sufficient to probe the velocity structures of molecular clouds and to observe the hyperfine structure of molecular transitions. The FFT2G supports Universal Serial Bus (USB) connections for data dumps and two Bayonet Neill-Concelman (BNC) inputs for accumulation control; data buffers accumulate data and switch alternately in on-the-fly (OTF) mode. The OTF mode can run fast by direct command via the BNC inputs. The minimum stable dump time is 200 ms during a data transfer. The BNC inputs are customized to control the switching of FFT2G memory for accurate signal integration, which is especially important when using the OTF mode. With a change of the firmware, the bandwidth of the module can be expanded to 2 GHz, albeit at the cost of reducing the number of input ports from eight to two.

### 2.4. Operating System and Data Reduction

The operating system VxWorks 6.9 is used for controlling the telescope and handling observation programs which operate on several boards connected by a VME-bus system. A Motorola CPU board (MVME-6100) is the main computer. The VME 2510 model used in this case is a 64-bit TTL input/output board. It controls the integration process on the FFT2G directly. GPS is supported with a BC637VME board. The VME-5565 model board is a reflective memory board that is connected to a host Linux (Ubuntu 10.04.4 LTS) computer onto which LMTMC-TRAO, a rebuilt version of the Large Millimeter Telescope Monitor and Control (LMTMC) system developed by the FCRAO, is installed. The host computer works in conjunction with the VxWorks system and can manage the observations. The backend computer manages FFT2G on Ubuntu 14.04.5 LTS. Transmission Control Protocol (TCP) and User Datagram Protocol (UDP) socket programming is used to communicate with the VxWorks system. The frontend system runs on a PC-DOS 2000 computer. Most programs managing the receiver are based on Fortran 70.

Observations can be made either in a pointing mode with position switching (PS) or in an on-the-fly (OTF) mode. For OTF observations, data reduction is handled mainly by OTFTOOL which has been modified to work on the current operating system and with the GILDAS[2] software package. In this program, there are four types of data convolution functions on a regular grid: a Gaussian-tapered Jinc function (Jinc×Gauss), a Gaussian-tapered Sinc function (Sinc×Gauss), a Sinc function, and Gaussian functions (Mangum et al. 2007; Sawada et al. 2008). The OTF map is computed from the convolved data and stored as a CLASS file or a FITS data cube on a regular grid.

**Table 2**
Jupiter OTF Observations

| Observation date [UT] | Size[a] [″] | $\nu$(IF1)[b] [GHz] | $\nu$(IF2)[b] [GHz] |
|---|---|---|---|
| 2016 Mar 11 1400 | 44.4 | 115.271 | 110.201 |
| 2016 Mar 21 1530 | 44.2 | 86.243 | 98.000 |
| 2017 Mar 02 1500 | 42.3 | 86.243 | 98.000 |
| 2017 Mar 02 1700 | 42.3 | 115.271 | 110.201 |

[a] Angular size of Jupiter at the time of the observation, from the Korean Astronomical Almanac.
[b] Frequency observed using the given intermediate frequency (IF).

## 3. TELESCOPE BEAM SIZES AND EFFICIENCIES

Beam parameters were measured by observing Jupiter with the SEQUOIA-TRAO receiver. Jupiter is widely used as a primary calibrator for infrared and radio observations as it is one of the brightest celestial objects at those frequencies and its whole-disk brightness temperature is well known and stable (Weiland et al. 2011).

In February 2017, the new radome was installed. Since the first installation of the radome in 1985, the membrane of the old radome had worn out and had begun to lose its ability to protect the telescope. Thus, we compare the beam parameters before and after the installation of the new radome to assess the effects of the radome on the beam parameters. Radio continuum observations of Jupiter were carried out in March 2016 and in March 2017. We obtained continuum maps of Jupiter using the OTF mapping mode by scanning in the azimuth direction at four frequencies: 86.2, 98.0, 110.2, and 115.2 GHz. We mapped an $8' \times 8'$ area, which is large enough to cover Jupiter with all receiver pixels. Table 2 summarizes the observations.

Figure 3 shows the maps resulting from combining the data from all 16 pixels at all four frequencies and for both years. The images clearly show the expected decrease in the beam size with increasing frequency. The beam patterns measured in 2016 have a more asymmetric shape, showing elongation in the elevation direction by approximately 20%. The beam patterns became more symmetric in 2017 after adjusting the alignment between

[1] https://www.omnisys.se/product/fft-spectrometer

[2] https://www.iram.fr/IRAMFR/GILDAS

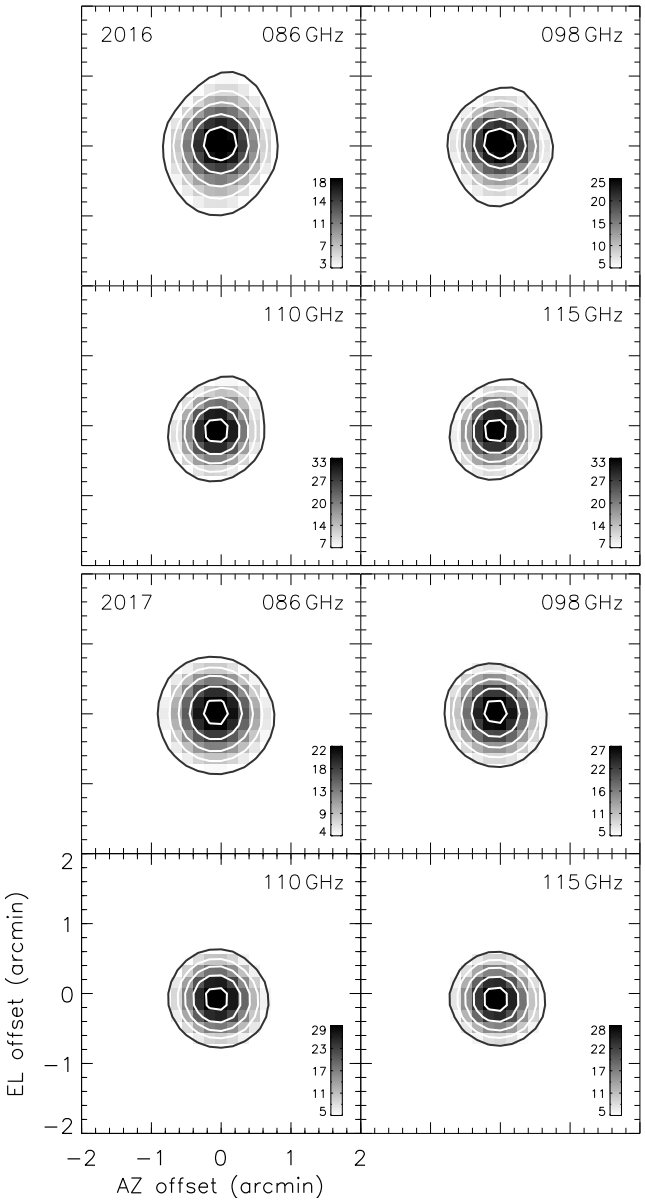


**Figure 3.** Continuum images of Jupiter obtained in 2016 (top set of panels) and in 2017 (bottom set of panels) at 86, 98, 110, and 115 GHz. Each image was obtained by averaging the continuum images from the 16 horns of the SEQUOIA-TRAO receiver. The contour levels are 20%, 35%, 50%, 70%, and 90% of the peak intensity. The gray scale encodes antenna temperatures $T_A^\star$ in Kelvin.

the receiver and the sub-reflector. The replacement of the servo system helped to improve the pointing accuracy in both the azimuth and elevation directions. From 2016 to 2017, the ellipticity of the beam reduced from 0.15 to 0.05. Figure 4 shows the individual beam patterns for all 16 pixels, as obtained with observations of Jupiter at 110 GHz in 2017. Else than in 2016, the beam patterns measured in 2017 do not show systematic asymmetries. The continuum maps of Jupiter show position offsets, which are however confined to the pointing errors of $< 5''$.

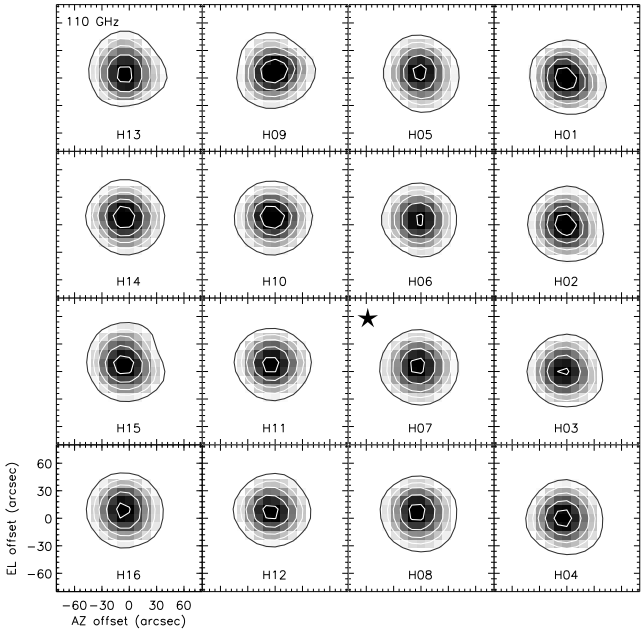


**Figure 4.** Continuum images of Jupiter from all 16 horns, taken at 110 GHz in 2017. Contour levels are 20%, 35%, 50%, 70%, and 90% of the peak intensity, the gray scale indicates values of $T_A^\star$ from 6 K to 30 K. A star marks the reference pixel for pointing and position switching observations.

In order to determine the efficiencies of the radio telescope, the antenna temperature ($T_A^*$) and the half power beam width (HPBW, $\theta_0$) averaged over major and minor axes were measured by fitting each image of Jupiter with a two-dimensional Gaussian function. Assuming that the main beam pattern has a Gaussian shape and that Jupiter is a circular disk with uniform brightness temperatures, the size of the main beam ($\theta_M$), the aperture efficiency ($\eta_A$), and the main-beam efficiency ($\eta_B$) are determined with the following equations (Baars 1973; Roh & Jung 1999; Koo et al. 2003; Lee et al. 2011):

$$\theta_M = \left( {\theta_0}^2 - \frac{\ln 2}{2}\, {\theta_S}^2 \right)^{1/2} , \tag{1}$$

$$\eta_A \equiv \frac{A_e}{A_p} = \frac{\lambda^2}{A_p \Omega_A} = \frac{\lambda^2 T_A^*}{A_p T_B \Omega_s} , \tag{2}$$

$$\eta_B \equiv \frac{\Omega_s}{\Omega_A} = \frac{\Omega_M T_A^*}{T_B \Omega_s} = \frac{\Omega_M A_p}{\lambda^2} \eta_A , \tag{3}$$

$$\Omega_s = \Omega_M \left[ 1 - \exp\left( -\ln 2 \left( \frac{\theta_s}{\theta_M} \right)^2 \right) \right] , \tag{4}$$

$$\Omega_M = 1.133\, \theta_M^2 . \tag{5}$$

**Table 3**
TRAO telescope parameters measured in 2016 and 2017

| Year | Frequency [GHz] | $\theta_M$ [″] | $\eta_A$ [%] | $\eta_B$ [%] |
|---|---|---|---|---|
| 2016 | 86.243 | 60 ± 2 | 31 ± 1 | 37 ± 2 |
| | 98.000 | 54 ± 1 | 35 ± 1 | 42 ± 2 |
| | 110.201 | 49 ± 1 | 39 ± 1 | 49 ± 2 |
| | 115.271 | 47 ± 1 | 36 ± 1 | 46 ± 1 |
| 2017 | 86.243 | 57 ± 2 | 43 ± 1 | 45 ± 2 |
| | 98.000 | 52 ± 1 | 42 ± 1 | 48 ± 2 |
| | 110.201 | 49 ± 1 | 37 ± 1 | 46 ± 2 |
| | 115.271 | 47 ± 1 | 33 ± 1 | 41 ± 2 |

Here, $A_e$, $A_p$, $T_B$, and $\theta_s$ are the effective and physical area of the antenna, the brightness temperature, and the angular size of the source, respectively; $\Omega_s$, $\Omega_M$, and $\Omega_A$ are the solid angles of the source, the main beam, and the antenna, respectively. We assumed the brightness temperature of Jupiter in all frequency bands to be 173.1±0.1 K (Joiner & Steffes 1991; Weiland et al. 2011).

Table 3 shows the measured main beam size, aperture efficiency, and main-beam efficiency as observed in 2016 and 2017 using Equations (1) to (3). The averaged beam FWHMs are 60″, 54″, 49″, and 47″ in 2016, and 57″, 52″, 49″, and 47″ in 2017 at 86, 98, 110, and 115 GHz, respectively. The slight differences in the main beam sizes between the two seasons are mainly due to the elongations in radio continuum images at low frequencies. The measured aperture efficiencies are 31%, 35%, 39%, and 36% in 2016, and 43%, 42%, 37%, and 33% in 2017 at 86, 98, 110, and 115 GHz, respectively. The main-beam efficiencies are 37%, 42%, 49%, and 46% in 2016, and 45%, 48%, 46%, and 41% in 2017 at 86, 98, 110, and 115 GHz, respectively. Table 4 shows the beam parameters measured in 2017 for all 16 receiver horns as function of frequency.

Figure 5 displays the aperture and main-beam efficiencies as function of frequency, separately for 2016 and 2017. The errors on the efficiencies largely originate from measurement errors given by the standard deviations of the model fits. From Figure 5, we find that both the aperture and the main-beam efficiencies increase with frequency at least up to 115 GHz in the 2016 observations. However, the aperture and main-beam efficiencies measured in 2017 show different trends. The systematic differences between 2016 and 2017 are due to the replacement of the radome; the changes in shape and membrane of the radome modified the transmissivity as function of frequency. The transmission coefficients of the old and new radome components are shown in the bottom panel of Figure 5, indicated by dotted lines. The transmission coefficient of the old membrane was calculated assuming plane wave transmission through a 0.75-mm-thick slab (Balanis 1989); the dielectric constant and loss tangent of the slab were 2.8 and 0.011, respectively. The transmission coefficient of the new membrane was provided by the manufacturer. The variation of the transmission

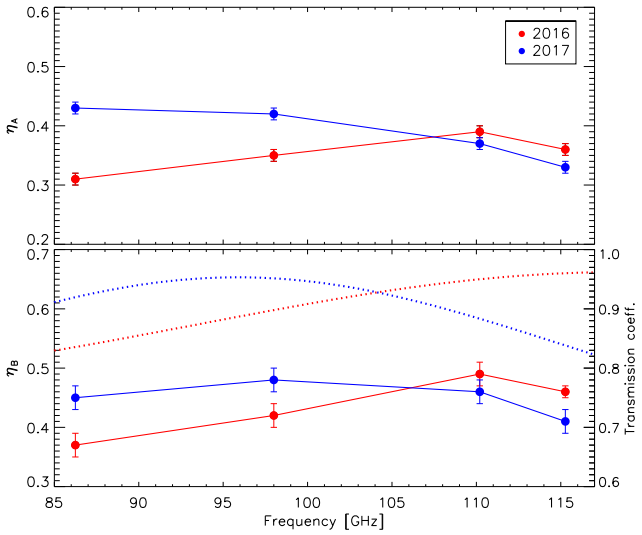


**Figure 5.** Antenna efficiencies before (2016, red) and after (2017, blue) the replacement of the radome. Both panels display the aperture and main-beam efficiencies at four frequency bands. The dotted lines in the lower panel indicate the transmission coefficients for the membranes of the old (red) and new (blue) radomes.

coefficients with frequency of the old (ESSCOLAM$^{TM}$6) and new (ESSCOLAM$^{TM}$10) membranes matches the trends observed for the efficiencies. The efficiencies of the new membrane are higher than those of the old one by 8% at 86 GHz, whereas for the old membrane, the efficiency is 12% higher than that of the new one at 115 GHz, implying that the efficiencies of the antenna improved below 105 GHz and deteriorated slightly above 105 GHz. In addition, the beam efficiencies are highest at the frequencies where the transmission coefficients peak.

## 4. SPECTRAL LINE OBSERVATIONS

In Figure 6, we present spectra of Orion-KL and IRC 10216 observed in the position switching mode. These objects are standard calibrators for spectroscopic observations at millimeter wavelengths. The observations were performed at 86.243 GHz (SiO $J = 2 - 1$, $v = 1$), 97.980 GHz (CS $J = 1 - 0$), 110.201 GHz ($^{13}$CO $J = 1 - 0$), and 115.271 GHz ($^{12}$CO $J = 1 - 0$) for Orion-KL, and at 86.243, 110.201, and 115.271 GHz for IRC 10216. Each spectrum was obtained by observing 7.5 min on source and 7.5 min off source, and thus for a total exposure time of 15 min. The system temperature ranged from 155 K to 575 K depending on the observing frequency. At a spectral resolution of 15 kHz, the rms noise levels of the spectra were 0.09 K and 0.31 K at 86 GHz and 115 GHz for Orion-KL, and 0.08 K and 0.27 K at 97 GHz and 115 GHz for IRC10216, respectively. These values are consistent with the values expected from the system noise temperatures and integration times. We compared the brightness temperatures of the TRAO radio telescope toward Orion-KL at $^{13}$CO $J = 1 - 0$ and $^{12}$CO $J = 1 - 0$ with those of the FCRAO 13.7-m radio telescope (Ladd et al. 2005)

**Table 4**
Beam parameters for all 16 receiver horns obtained from observations of Jupiter in 2017

| Frequency [GHz] | Horn (#) | $\theta_M$ [″] | $\eta_A$ [%] | $\eta_B$ [%] | Horn (#) | $\theta_M$ [″] | $\eta_A$ [%] | $\eta_B$ [%] | Horn (#) | $\theta_M$ [″] | $\eta_A$ [%] | $\eta_B$ [%] | Horn (#) | $\theta_M$ [″] | $\eta_A$ [%] | $\eta_B$ [%] |
|---|---|---|---|---|---|---|---|---|---|---|---|---|---|---|---|---|
| 86.243 | 1 | 58 | 42 | 46 | 5 | 57 | 46 | 48 | 9 | 56 | 43 | 43 | 13 | 58 | 44 | 48 |
| | 2 | 59 | 44 | 49 | 6 | 57 | 45 | 46 | 10 | 55 | 41 | 41 | 14 | 57 | 43 | 46 |
| | 3 | 58 | 45 | 50 | 7 | 57 | 42 | 43 | 11 | 56 | 44 | 45 | 15 | 57 | 42 | 44 |
| | 4 | 58 | 42 | 46 | 8 | 56 | 43 | 44 | 12 | 56 | 45 | 45 | 16 | 58 | 40 | 44 |
| 98.000 | 1 | 53 | 42 | 49 | 5 | 52 | 41 | 47 | 9 | 51 | 45 | 48 | 13 | 53 | 43 | 49 |
| | 2 | 54 | 40 | 49 | 6 | 52 | 42 | 47 | 10 | 50 | 44 | 46 | 14 | 52 | 44 | 49 |
| | 3 | 54 | 41 | 50 | 7 | 52 | 42 | 47 | 11 | 51 | 43 | 46 | 15 | 52 | 43 | 47 |
| | 4 | 54 | 42 | 51 | 8 | 52 | 43 | 49 | 12 | 51 | 44 | 47 | 16 | 52 | 42 | 48 |
| 110.201 | 1 | 48 | 40 | 48 | 5 | 49 | 36 | 46 | 9 | 47 | 42 | 48 | 13 | 48 | 38 | 47 |
| | 2 | 48 | 39 | 47 | 6 | 48 | 36 | 44 | 10 | 47 | 40 | 47 | 14 | 48 | 39 | 48 |
| | 3 | 48 | 36 | 43 | 7 | 50 | 37 | 48 | 11 | 47 | 38 | 45 | 15 | 50 | 38 | 49 |
| | 4 | 48 | 38 | 46 | 8 | 49 | 37 | 47 | 12 | 48 | 37 | 44 | 16 | 49 | 37 | 47 |
| 115.271 | 1 | 46 | 35 | 42 | 5 | 48 | 33 | 44 | 9 | 45 | 35 | 41 | 13 | 47 | 33 | 41 |
| | 2 | 46 | 34 | 42 | 6 | 45 | 33 | 39 | 10 | 44 | 35 | 39 | 14 | 47 | 33 | 42 |
| | 3 | 45 | 36 | 42 | 7 | 48 | 31 | 42 | 11 | 45 | 33 | 40 | 15 | 47 | 32 | 42 |
| | 4 | 46 | 36 | 44 | 8 | 48 | 33 | 43 | 12 | 45 | 34 | 41 | 16 | 48 | 32 | 42 |

Errors in beam sizes, antenna efficiencies, and beam efficiencies are about 10%.

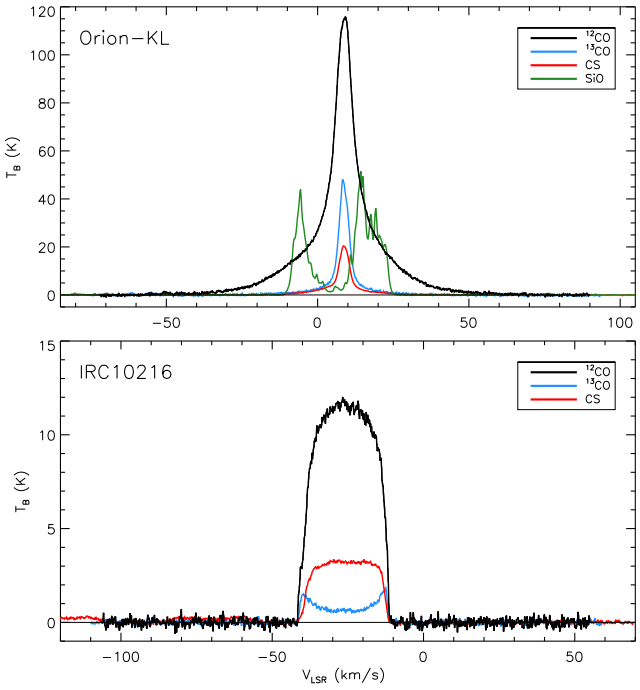


**Figure 6.** Spectral lines of Orion-KL and IRC10216, displayed as brightness temperature $T_B$ as function of line-of-sight velocity. *Top panel:* Orion-KL lines at 115.271 ($^{12}$CO), 110.201 ($^{13}$CO), 97.980 (CS), and 86.243 GHz (SiO). The $^{13}$CO line profile has been multiplied by two along the $T_B$ axis to prevent overlap with the CS line. *Bottom panel:* $^{12}$CO, $^{13}$CO, and CS observed toward IRC 10216. The coordinates of the observed position were RA = $05^h\ 35^m\ 14^s.5$ and Dec = -5° 22′ 30″.7 (J2000) for Orion-KL, and RA = $9^h\ 47^m\ 57^s.4$ and Dec = 13° 16′ 43″.5 for IRC 10216, respectively.

and found them to coincide with each other within 10%; discrepancies can be explained by the errors in main beam efficiency and pointing.

## 5. SUMMARY

After renewing several parts of the telescope system, including the receiver system, backend, servo system, operating system, and radome, the performance of the TRAO 13.7-m radio telescope is found to have improved substantially. The newly installed 16-pixel receiver SEQUOIA-TRAO shows system noise temperatures of 150–300 K in the frequency range 86–110 GHz and <450 K at 115 GHz; this a substantial improvement over the performance of the previous system. The combination of SEQUOIA-TRAO and the FFT2G spectrometer makes it possible to obtain 32 line spectra, from simultaneous observations at two frequencies with 16 receiver horns, with bandwidths of 62.5 MHz sampled by 4096 channels. The new servo system provides for a pointing error of $< 5''$ in both azimuth and elevation.

Radio continuum observations of Jupiter in OTF find beam sizes 57″–47″ over the frequency range 86–115 GHz. The aperture efficiencies are measured to be 31%, 35%, 39%, and 36% in 2016, and 43%, 42%, 37%, and 33% in 2017 at 86, 98, 110, and 115 GHz, respectively. The main-beam efficiencies are 37%, 42%, 49%, and 46% in 2016, and 45%, 48%, 46%, and 41% in 2017 at 86, 98, 110, and 115 GHz, respectively. Comparing the observations from 2016 to those from 2017, the efficiencies change substantially due to different transmission coefficients of the old and new radome membranes. We also presented line spectra of Orion-KL and IRC 10216 to demonstrate the performance of the new spectrometer.

With the new equipment and observing systems, the TRAO 13.7-m radio telescope is able to provide high-quality observational data. The remote observation mode was recently tested successfully. In addition,

tests of a wideband (bandwidth 2 GHz) backend system for two pixels are ongoing. From the beginning of 2020, we plan wideband observations of high-velocity sources and various molecular line observations with single exposures. We will also continue to provide updated information pertaining to the efficiencies and the equipment of the TRAO telescope on our homepage (https://radio.kasi.re.kr/trao) for user support purposes.

## Acknowledgments

We would like to thank the anonymous referees for constructive comments and suggestions. C.W.L. was supported by the National Research Foundation of Korea (grant NRF-2019R1A2C1010851).

## References

Baars, J. W. M. 1973, The Measurement of Large Antennas with Cosmic Radio Sources, IEEE Trans. Antennas Propag., 21, 461

Balanis, C. A. 1989, Advanced Engineering Electromagnetics (Hoboken: John Wiley & Sons)

Cho, S.-H., Chung, H.-S., Kim, H.-R., et al. 1998, Observations of SiO ($v = 0, 1, 2$) $J = 3-2$ and $J = 2-1$ Emission in Late-Type Stars, ApJS, 115, 277

Cho, S.-H., Lee, C. W., & Park, Y.-S. 2007, First Detection of the SiO ($v = 3$, $J = 2-1$) Maser Emission from $\chi$ Cygni, ApJ, 657, 482

Erickson, N. R., Goldsmith, P. F., Novak, G., et al. 1992, A 15 Element Focal Plane Array for 100 GHz, IEEE Trans. Microw. Theory Tech., 40, 1

Erickson, N. R., Grosslein, R. M., Erickson, R. B., & Weinreb, S. 1999, A Cryogenic Focal Plane Array for 85–115 GHz Using MMIC Preamplifiers, IEEE Trans. Microw. Theory Tech. 47, 2212

Joiner, J., & Steffes, P. G. 1991, Modeling of Jupiter's Millimeter Wave Emission Utilizing Laboratory Measurements of Ammonia ($NH_3$) Opacity, JGR, 96, 17

Koo, B.-C., Park, Y.-S., Hong, S. S., et al. 2003, Performance of the SRAO 6-Meter Radio Telescope, JKAS, 36, 43

Koo, B.-C., Rho, J., Reach, W. T., et al. 2001, Shocked Molecular Gas in the Supernova Remnant HB 21, ApJ, 552, 175

Ladd, N., Purcell, C., Wong, T., et al. 2005, Beam Size, Shape and Efficiencies for the ATNF Mopra Radio Telescope at 86–115 GHz, PASA, 22, 62

Lee, C., Jung, J. H., Kang, H. W., et al. 2014, Panel Adjustment of the TRAO 13.7-m Antenna Using Photogrammetry, PKAS, 29, 53

Lee, S.-S., Byun, D.-Y., Oh, C. S., et al. 2011, Single-Dish Performance of KVN 21-m Radio Telescopes: Simultaneous Observations at 22 and 43 GHz, PASP, 123, 1398

Lee, Y., Kim, Y. S., Kim, H.-G., et al. 2014, Two Molecular Clouds with Anomalous Velocities in the Galactic Anticenter, JKAS, 47, 319

Loughnane, R. M., Redman, M. P., Thompson, M. A., et al. 2012, Observations of HCN Hyperfine Line Anomalies towards Low- and High-mass Star-forming cores, MNRAS, 420, 1367

Mangum, J. G., Emerson, D. T., & Greisen, E. W. 2007, The On-The-Fly Imaging Technique, A&A, 474, 679

Roh, D.-G., & Jung, J. H. 1999, Characteristics of TRAO 14m Radio Telescope (1999), PKAS, 14, 123

Sawada, T., Ikeda, N., Sunada, K., et al. 2008, On-The-Fly Observing System of the Nobeyama 45-m and ASTE 10-m Telescopes, PASJ, 60, 445

Weiland, J. L., Odegard, N., Hill, R. S., et al. 2011, Seven-year Wilkinson Microwave Anisotropy Probe (WMAP) Observations: Planets and Celestial Calibration Sources, ApJS, 192, 19